




## Structure, mechanical properties and surface morphology of the snapping shrimp claw

Zhihui Qian<sup>1</sup>, Mingming Yang<sup>1</sup>, Liang Zhou<sup>1</sup>, Jing Liu<sup>1</sup>, Riaz Akhtar<sup>2</sup>, Chunbao Liu<sup>1,\*</sup>, Yan Liu<sup>1</sup>, Luquan Ren<sup>1</sup>, and Lei Ren<sup>1,3,\*</sup> 

<sup>1</sup>Key Laboratory of Bionic Engineering, Jilin University, Changchun 130022, People's Republic of China

<sup>2</sup>Centre for Materials and Structures, School of Engineering, University of Liverpool, Liverpool L69 3GH, UK

<sup>3</sup>School of Mechanical, Aerospace and Civil Engineering, University of Manchester, Manchester M13 9PL, UK

Received: 6 March 2018

Accepted: 24 April 2018

Published online:

4 May 2018

© Springer Science+Business Media, LLC, part of Springer Nature 2018

### ABSTRACT

The snapping shrimp preys by rapidly closing its snapping claw to generate a fast water jet, creating a shockwave that bombards the nearby prey and other shrimp. This behaviour has led to considerable interest and research. However, the structure, surface morphology and mechanical properties of the snapping claw are unreported. We used a combination of techniques including scanning electron microscopy and nanoindentation to characterise the claw. These measurements were coupled with computational fluid dynamics (CFD) to understand how the microstructure contributes to drag reduction. We found that cone-shaped micropapillae, rhombic dents and short straight stripes were hierarchically distributed on the surface of the claw. CFD simulation showed that the micropapillae units changed the interaction between the turbulent and the wall from sliding friction to rolling friction, resulting in tire-shaped vortices. This also reduced the turbulent kinetic energy in the near-wall region, thereby contributing to drag reduction. The cross section of the claw revealed four layers comprising an epicuticle, exocuticle, endocuticle and a membranous layer. The exocuticle is composed of chitin fibres arranged vertically in a lamellar fashion and the endocuticle has a Bouligand-type structure. This special structure provides the snapping shrimp with good mechanical resistance during rapid closure. Both modulus and hardness decreased from the outermost epicuticle to the innermost membranous layer. The gradient modulus and hardness may help to suppress microcracks at the interfaces between different layers. The findings improve our understanding of the unique mechanism of the snapping claw and may lead to the development of novel biomimetic materials with enhanced drag reduction, impact and crack resistance properties.

Address correspondence to E-mail: liuchunbao15@hotmail.com; renlei15@hotmail.com

## Introduction

The snapping shrimp (*Alpheus heterochaelis*), commonly known as the pistol shrimp, has two claws, a small pincer and an enormous snapper. The specialised snapper, which may be on either the right or the left and can grow up to half of the shrimp's body length, has a protruding plunger on the dactyl (mobile) and a matching socket in the propus (immobile) side [1]. Extremely rapid closure of the snapper claw can produce a fast, well-focused water jet in about 600–750  $\mu\text{s}$  [1–3]. During the closure, the protruding plunger is driven into the propus socket, displacing water that escapes through a narrow anterior groove [2]. The high-velocity water jet resulting from the rapid closure first loses and then gains pressure, causing a large air cavitation bubble that swells and collapses with a loud crackling noise [1–3]. The imploding bubble generates shock waves that can easily stun or even kill nearby small prey and ward off other shrimps and small crabs [2–4]. These unique properties have attracted great interest in studying the snapping shrimp claw [1–10].

Over past decades, many experimental studies have investigated how the snapping shrimp claw functions [1–5]. Prior to snapping, the dactyl of the shrimp is first cocked at about  $100^\circ$  by co-contracting both the opening and closing muscles of the snapping claw. This generates tension until a second closer muscle contracts, setting the dactyl off with incredible force [6]. Then, the plunger is slammed into the socket with a high velocity of 108 km/h, resulting in a fast water jet [7]. To gain more insight into the biophysical characteristics of the water jet, the jets of tethered snapping shrimp have been visualised and analysed using standard and high-speed video recording [2]. The water jet distances, width, velocities and their correlations with claw cock duration, snapper claw length and volume have been well illustrated [2]. During the rapid claw closure, a short and intense sound as high as 190–210 dB is emitted, which originates from the collapse of cavitation bubbles [1]. The frequency spectrum of the snap sound is broad, ranging from tens of hertz to  $> 200$  kHz [8]. The snapping noise was therefore used as a source for creating pictorial images of objects in the ocean by ensonification [9] and was also used to drown out submarine-detecting sonar [7]. In addition to the snapping sound, measurements have shown

that the collapse of cavitation bubbles generates an intense flash of light and temperature of at least 5000 K, which is nearly as hot as the surface of the sun (about 5770 K) at the point of collapse [5, 10]. The resulting shockwave bombards the nearby prey and other shrimp [11], which means that the snapping shrimp skeleton, especially the claw, needs to be impact resistant. A recent evolutionary analysis based on observation of the structure and musculature of the claw joint found two new joint configurations, a slip joint and a torque reversal joint, that contribute to ultrafast movement of the snapping claw [12].

Although previous studies have greatly improved our understanding of the closure motion pattern, snapping sound and shrimpluminescence of the snapping claw, little is known about its microstructure, mechanical properties and surface morphology and their potential biological functions, which may provide important information for the development of novel biomimetic materials with superior properties such as impact and crack resistance and drag reduction.

The objective of this study was to investigate the microstructural, surface morphological, material and mechanical properties of the snapping claw using field emission scanning electron microscope (FESEM), energy-dispersive X-ray spectroscopy (EDS), nanoindentation and computational fluid dynamics (CFD) simulation, and to relate these structural and material properties to the biological function of the claw.

## Materials and methods

### Preparation of snapping shrimp

Five living adult snapping shrimps were obtained from a local seafood market in Changchun, China. The snapping shrimps were housed in separate glass containers with a constant circulation of fresh sea water and were fed until the specimens were required.

### Microstructure, material composition and surface morphology measurement

The microstructure, material composition and surface morphology of the snapping claws were characterised using FESEM (XL-30, FEI Company, USA),

which was equipped with EDS (Genesis 2000, EDAX Company). Prior to measurement, the intact snapping claws were first taken off the shrimp's body. The soft tissue was then carefully removed.

The snapping claws were cleaned for 30 min in an ultrasonic cleaner (KQ-50DA, Kunshan ultrasonic instruments CO., LTD.) and then put in a vacuum freeze drying machine (FD-1C-50, Beijing Bo Kang laboratory instruments Medical Co., Ltd, China) for 24 h. Separate samples were cut from the snapping claw to observe the surface morphology and cross-sectional microstructure. For surface morphology measurements, the size of samples was approximately 5 mm × 5 mm × 0.5 mm (length × width × thickness). For cross-sectional observations, samples were obtained by immediately fracturing the snapping claw before examination. All samples were mounted on aluminium sample holders and coated with 20 nm of gold in a sputter coater (JFC-1600, JEOL Ltd.). Samples were measured with the secondary electron mode at 10, and 20 kV accelerating voltage. The material composition of the samples was also analysed by the EDS module of the FESEM.

### Measurement of mechanical properties

Whereas traditional uniaxial measurement can only provide overall mechanical property information, nanoindentation can provide site-specific data on the modulus and hardness of samples at the nano- or microscale. Therefore, 10 samples were prepared for nanoindentation measurement: 9 samples were cut from the dorsal surface of the immobile propus and 1 sample was cut from the mobile dactyl. Seven of the nine samples derived from the propus (labelled samples 1–7) were obtained along the longitudinal direction at 5-mm intervals. The other two were obtained from region B (samples B<sub>1</sub> and B<sub>2</sub>, respectively), as shown in Fig. 1. The sample cut from the dactyl was located in region A (sample A), also shown in Fig. 1. The seven longitudinal samples (samples 1–7) were used to investigate the distribution of surface hardness and elastic modulus from the tip of the propus to the end. Ten indentations were performed at each point. Sample B<sub>1</sub> was used to analyse the variation in hardness and modulus from the outer layer to the innermost layer of the claw. Samples A and B<sub>2</sub> were used to compare the local surface modulus of the dactyl and propus, respectively. Each sample was approximately 5 mm × 5

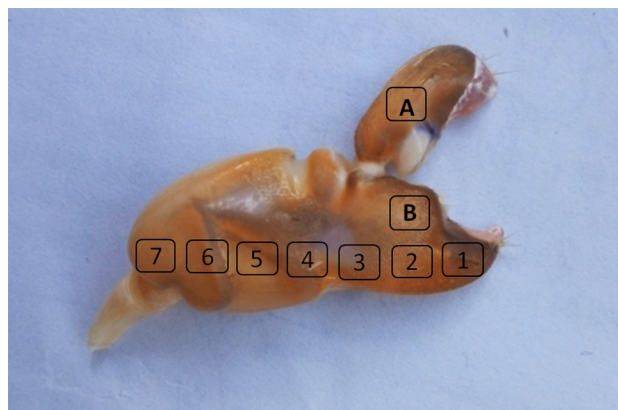


**Figure 1** Location of samples used for mechanical property measurements with nanoindentation. Region A is the mobile dactyl whereas the other samples (1–7 and B<sub>1</sub> and B<sub>2</sub>) are from the immobile propus.

mm × 0.5 mm (length × width × thickness). Prior to the nanoindentation measurement, sample B<sub>1</sub> was mounted in epoxy with the cross-sectional area exposed and then finely polished (MP-2, Shanghai Aidu Energy Technology Co., Ltd) [13]. All samples were cleaned for 30 min in an ultrasonic cleaner (KQ-50DA, Kunshan ultrasonic instruments Co. Ltd.) and dried at room temperature. A Keysight Nanoindenter (G200, Chandler, AZ, USA) was used for the nanoindentation measurements. A three-sided diamond pyramidal Berkovich tip was used for all experiments. The indentation data were analysed by the Oliver and Pharr method [14, 15].

### Computational fluid dynamics simulation

CFD models were built to understand how the surface morphology of the claw revealed by SEM contributes to drag reduction. The observed morphology is described in detail in Results in “Surface morphology” section. However, to describe the CFD approach clearly, it is noteworthy that cone-shaped micropapillae were observed on the surface of the dactyl and propus (see Fig. 3). The purpose of the CFD simulation was to investigate the effect of these micropapillae on water drag. To save computational costs, two 2D models, a micropapillae model and a smooth model, were constructed, as shown in Fig. 2a. The computational domains, A and B, are shown in Fig. 2a. The micropapillae model and smooth model were placed in domain B in the CFD simulations. The Integrated Computer Engineering and Manufacturing code for Computational Fluid Dynamics (version

16.0) was then used to generate mixed meshes of triangles and quadrangles for the computational domains. To capture more details of the fluid motion around the model, the meshes in the near-wall region of the two models were refined, as shown in Fig. 2b. Finally, 61,227 and 72,815 meshes were determined for domain B of the micropapillae model and smooth model, respectively (Fig. 2b). The Fluent software package (version 16.0) was used for the CFD simulation. In the simulation, the re-normalisation group  $k-\epsilon$  turbulent model and pressure-based solver were selected [15]. The model constants were all derived from previous studies [16–18]. Combined with the momentum equation and energy equation, Navier–Stokes equations can be solved [19]. The selected solvers and predefined parameters in the simulation are listed in Table 1.

## Results

### Surface morphology

Observations of the surface morphology characteristics of the dactyl and propus of the snapping claw were conducted using FESEM. Alongside the setae, which were mainly at the tip of the propus and dactyl (as shown in Fig. 3a–c), densely distributed cone-shaped micropapillae were found on the dorsal surface of snapping claw with a tilt angle of  $30^\circ \pm 5^\circ$ , as shown in Fig. 3. The basal diameter at the bottom and

**Table 1** The parameters used in the CFD simulations

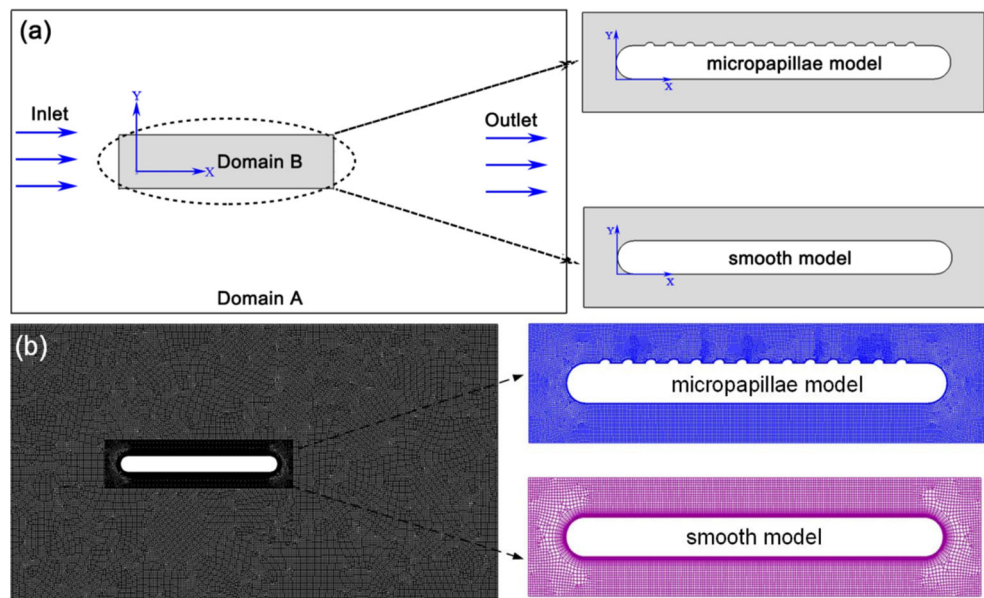
Parameters	Predefined value
Solver	Pressure-based
Turbulent model	RNG $k-\epsilon$ model
Inlet	Velocity inlet ( $30 \text{ ms}^{-1}$ )
Outlet	Outflow
Pressure–velocity coupling	PISO
Transient formulation	Bounded second-order implicit
Other term spatial discretisation	Second-order upwind
Time step size	0.0001 s
Number of time steps	2000

the height of the papilla were approximately 68–103 and  $33 \mu\text{m}$ , respectively. Alongside the cone-shaped micropapillae, rhombic dents and short straight stripes were present on the surface of the claw at a different length scale, as shown in Fig. 3d, e. The acute angle and the side length of the rhombic dents were approximately  $30^\circ$  and  $6\text{--}9 \mu\text{m}$ , respectively. The length and interval of the straight stripes were approximately 2.7–6.5 and  $1\text{--}2 \mu\text{m}$ , respectively.

### Characterisation of structure

As shown in Fig. 4, from the exterior to the interior, the exoskeleton of the snapping claw consists of four distinct layers. The outermost layer is the epicuticle, which is about  $2 \mu\text{m}$  thick and covered by a thin waxy layer. Following the epicuticle, the middle

**Figure 2** Schematic of **a** computational domains of CFD models and **b** computational meshes.



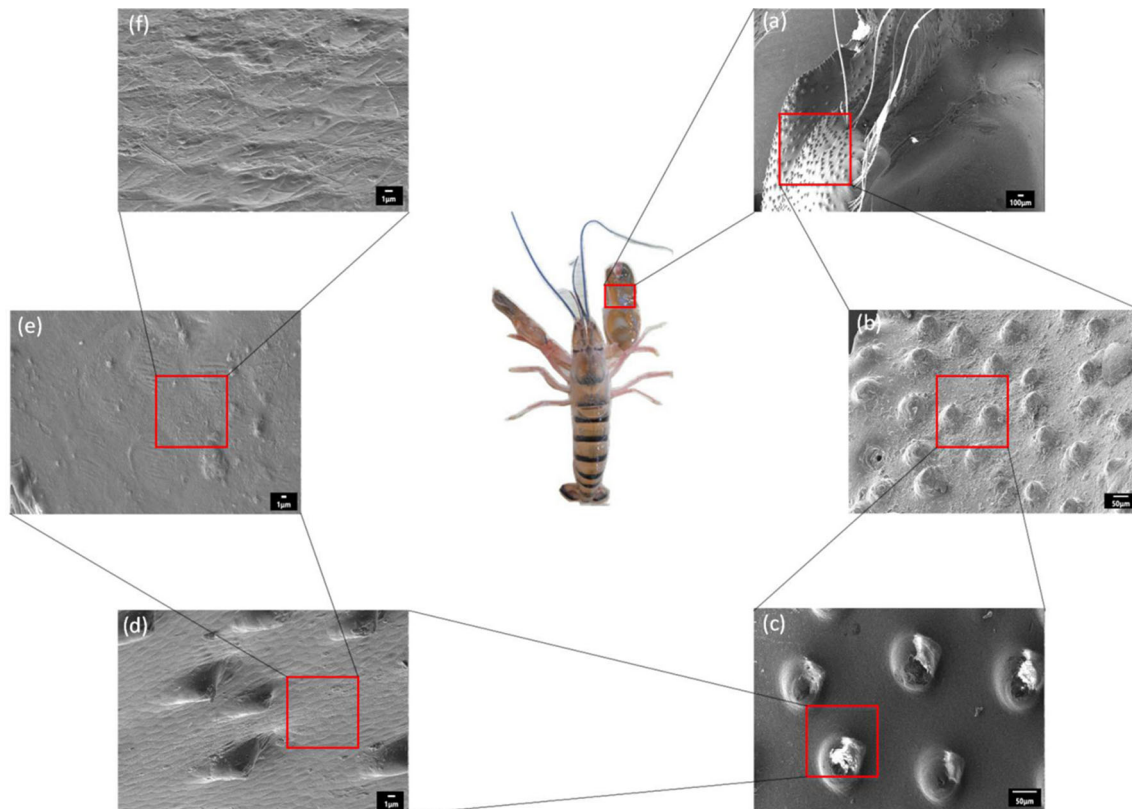


**Figure 3** SEM images of the surface morphology of a snapping claw at different magnifications. **a** Cone-shaped micropapillae are densely distributed on the dorsal surface of claw. Scale bar represents 100  $\mu\text{m}$ ; **b**, **c** magnified view of the micropapillae.

Scale bar represents 50  $\mu\text{m}$ ; **d** rhombic dents and short straight stripes on the surface of claw at a different length scales. Scale bar represents 1  $\mu\text{m}$ ; **e**, **f** different views of rhombic dents and short straight stripes. Scale bar represents 1  $\mu\text{m}$ .

second layer (with a thickness of about 75–130  $\mu\text{m}$ ) is the exocuticle, which comprises a distal smooth layer (Fig. 4a, b). The exocuticle mainly consists of chitin fibres arranged vertically in a lamellar fashion (as shown in Fig. 4c, d). The length of each lamella fibre is about 14  $\mu\text{m}$ , and the spacing between two fibre lamellas is about 0.6–1  $\mu\text{m}$ . Just below the exocuticle layer lies a 70–120- $\mu\text{m}$ -thick endocuticle, which consists of bundles of chitin fibres. The diameter of each bundle is about 300–900 nm. The fibres are arranged parallel to each other and form horizontal planes. These planes are stacked in a helicoid fashion, forming a twisted plywood or Bouligand structure (Fig. 4e, f). The fourth layer is the innermost membranous layer with a thickness ranging from 10 to 25  $\mu\text{m}$ . As shown in Fig. 4g, h, the innermost membranous layer consists of many densely stacked sub-layers, each approximately 450 nm thick.

### Material composition

EDS measurements were conducted to analyse the material composition of the snapping claw cuticle. Figure 5 shows the EDS spectra of surface samples derived from the dactyl and propus, respectively. Strong signals for calcium, oxygen and carbon were detected, indicating that these three elements are the main components of the surface of the cuticle in both the dactyl and propus, while sulphur, magnesium and phosphorus are present in minor amounts. The weight percentage of calcium in the dactyl was higher than that in the propus, which indicates that the surface of the former is more highly calcified than the latter. Figure 6 shows the qualitative EDS analysis of a cross-sectional sample derived from a propus. As shown in Fig. 6, calcium, oxygen and carbon are the main components of each layer, with smaller amounts of sulphur, magnesium and phosphorus, which is similar to the element distributions in the surface samples in Fig. 5. The weight percentage of

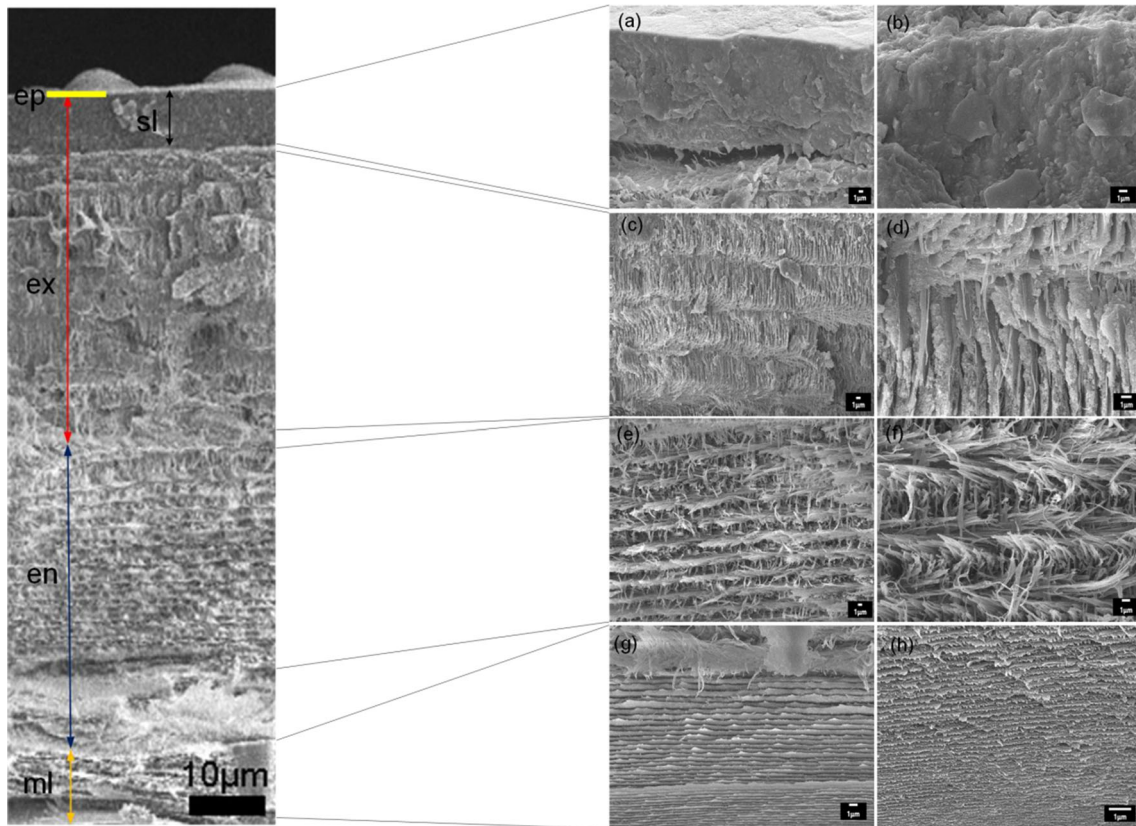


**Figure 4** Cross-sectional SEM image showing the microstructure of the snapping claw (dactyl and propus). On the left (A) is a thin epicuticle (ep) and an exocuticle layer (ex) that comprise a distal smooth layer (sl), an endocuticle (en) and a membranous layer (ml), and the scale bar is 10 μm; a shows the distal smooth layer of the exocuticle (sl) with the scale bar of 1 μm, and b shows the distal smooth layer at larger magnifications; c and d are the SEM

graphs of the exocuticle, except for the distal smooth layer, at different magnifications. The endocuticle layer consists of bundles of chitin fibres, which can be seen in (e) and (f), where the scale bar is 1 μm; g and h show the innermost membranous layer, which consists of many densely stacked sub-layers, and the scale bar is 1 μm.

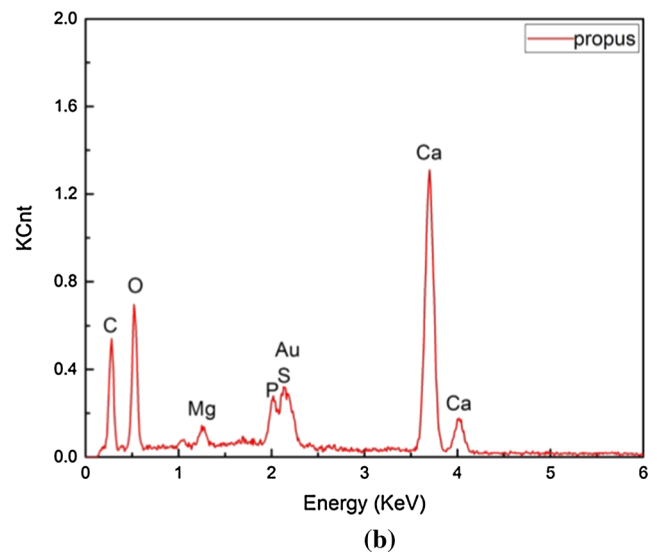
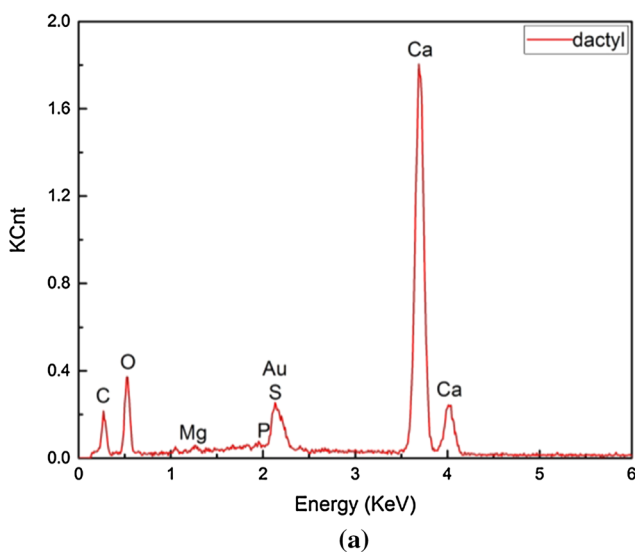


**Figure 5** EDS spectra of surface samples of cuticle derived from a the dactyl and b the propus.

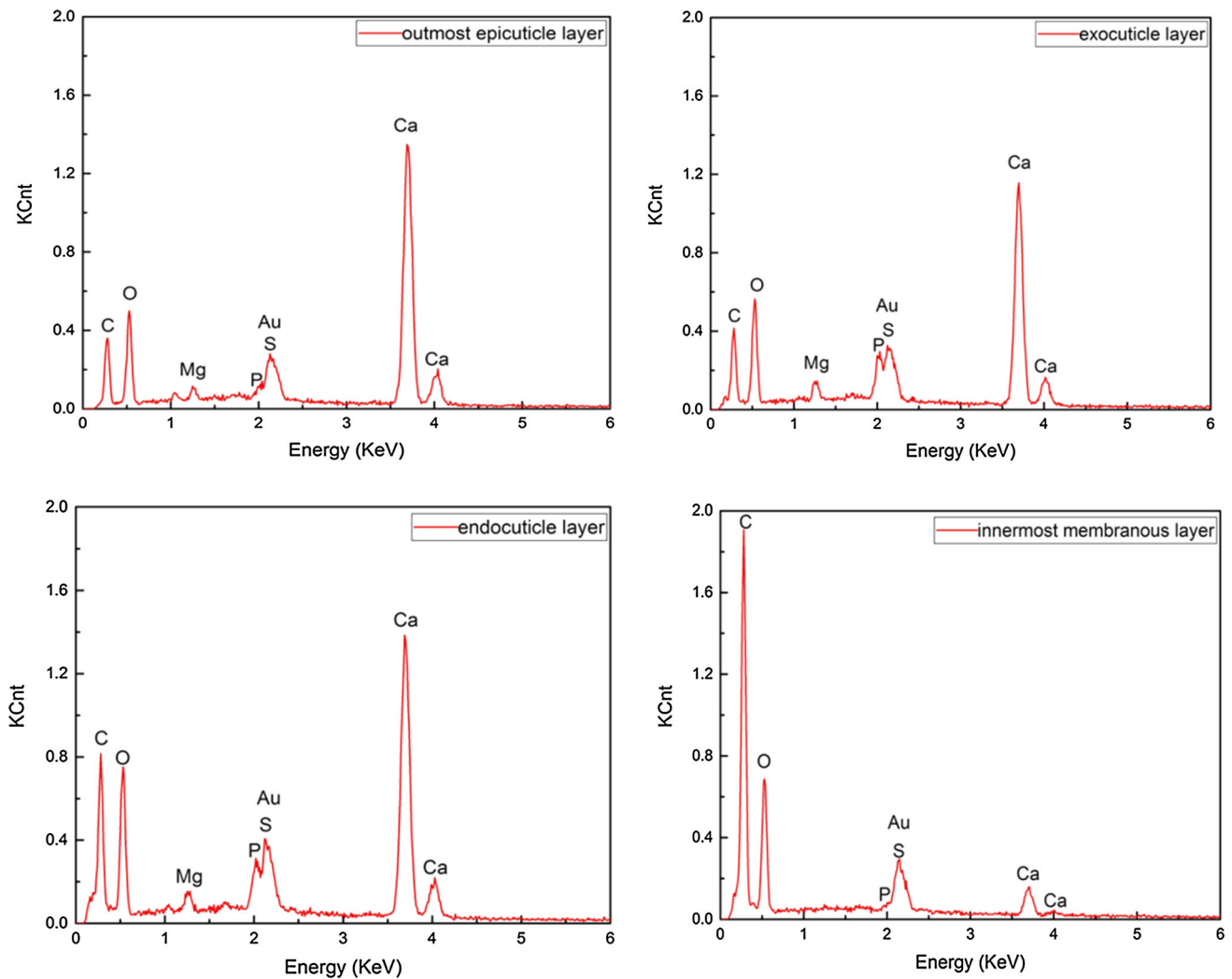


**Figure 6** Qualitative EDS analysis of the cross section of samples derived from the propus. EDS spectra of four different layers.

carbon increases from the outermost epicuticle to the innermost membranous layer, whereas that of calcium decreases, especially in the innermost membranous layer. These results reveal a gradient in the calcium and carbon contents between these four different layers and suggest that the outermost epicuticle layer is mainly impregnated with calcium salts, while the innermost membranous layer is less calcified. There was no difference in the weight percentages of oxygen, sulphur, magnesium and phosphorus among the layers.

### Mechanical properties

The local surface hardness and modulus of sample A (derived from the dactyl) and sample B<sub>2</sub> (derived from the propus) were obtained and compared. As

shown in Fig. 7a, the average local surface hardness of the dactyl and propus was  $1.26 \pm 0.81$  and  $0.41 \pm 0.47$  GPa, respectively. Figure 7b shows that the average modulus value of the dactyl was  $15.74 \pm 6.13$  GPa, while that of the propus was  $5.86 \pm 4.84$  GPa. The modulus and hardness of the dactyl surface were almost three times those of the propus. Hence, the dorsal surface of the dactyl is stronger and more able to resist external loads. This design (higher hardness and wear resistance on the surface) is widely found in nature [17]. Figure 8 shows the surface hardness and modulus of seven samples cut from the propus (as shown in Fig. 1) along the longitudinal direction. It can be seen that from the tip of the propus to the end, the hardness and modulus (in the locations of sample 1 and sample 6) are relatively low. The hardness peaks in the

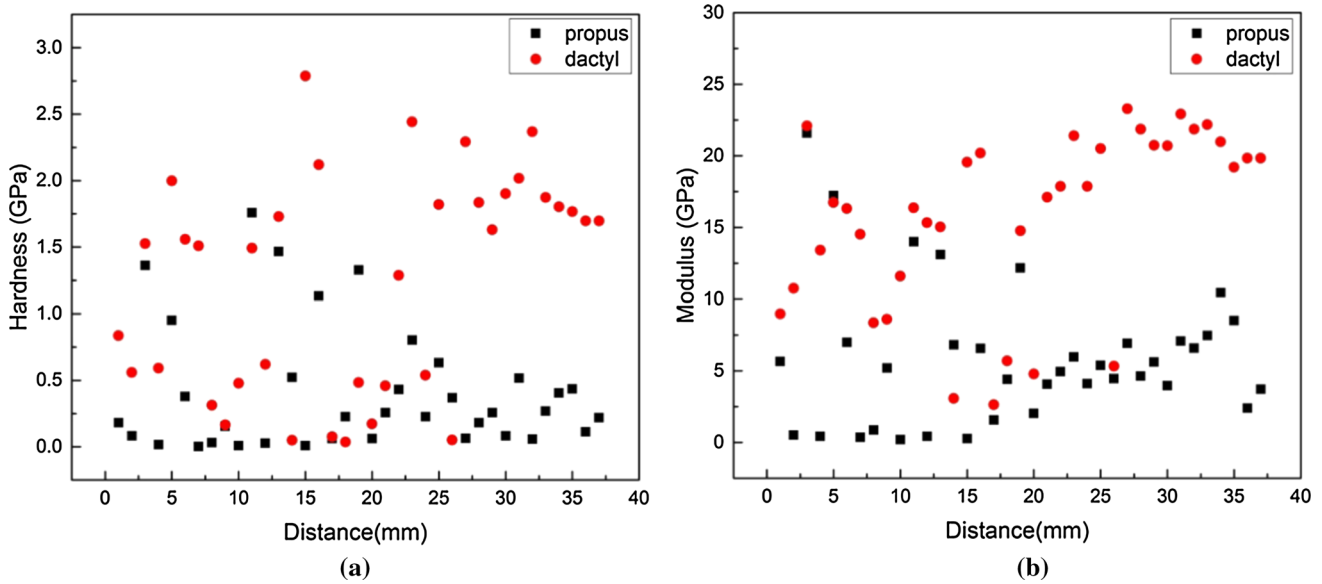


**Figure 7** Local surface hardness (a) and modulus (b) distribution across the dactyl and propus. **a** Comparison of the hardness between the propus (black squares) and dactyl (red squares); **b** comparison of the modulus between the propus (black squares) and dactyl (red squares).

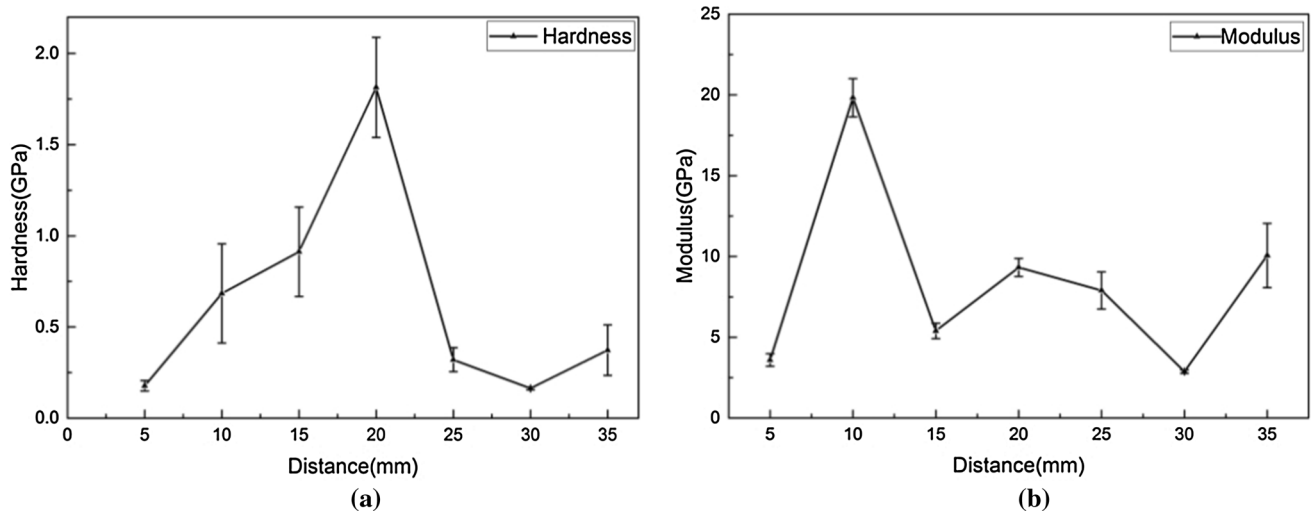


**Figure 8** Averages and standard deviations of the surface hardness (a) and modulus (b) of the propus along the longitudinal direction.

middle region (in the locations of samples 2, 3 and 4) and then decreases at the end. The largest average modulus value, 18 GPa, was found in the location of sample 2, and the modulus in the locations of samples 3, 4, 5 and 7 was around 8 GPa.

The cross section was investigated in addition to the nanoindentation measurement on the dorsal surface of the snapping claw. Due to the low thickness of the epicuticle and the membranous layer, only a limited number of indents could be performed in these regions. The mechanical properties including

the hardness and modulus were measured throughout the four layers (epicuticle, exocuticle, endocuticle and membranous layer) and compared, as shown in Fig. 9. The epicuticle was observed to be the hardest part of the skeleton with a modulus of  $19.73 \pm 6.59$  GPa and hardness of  $0.79 \pm 0.36$  GPa. The modulus was  $14.22 \pm 0.57$ ,  $9.22 \pm 2.04$  and  $4.16 \pm 2.36$  GPa for the exocuticle, endocuticle and membranous layer, respectively. The hardness was  $0.42 \pm 0.04$ ,  $0.33 \pm 0.05$  and  $0.21 \pm 0.17$  GPa for the exocuticle, endocuticle and membranous layer,



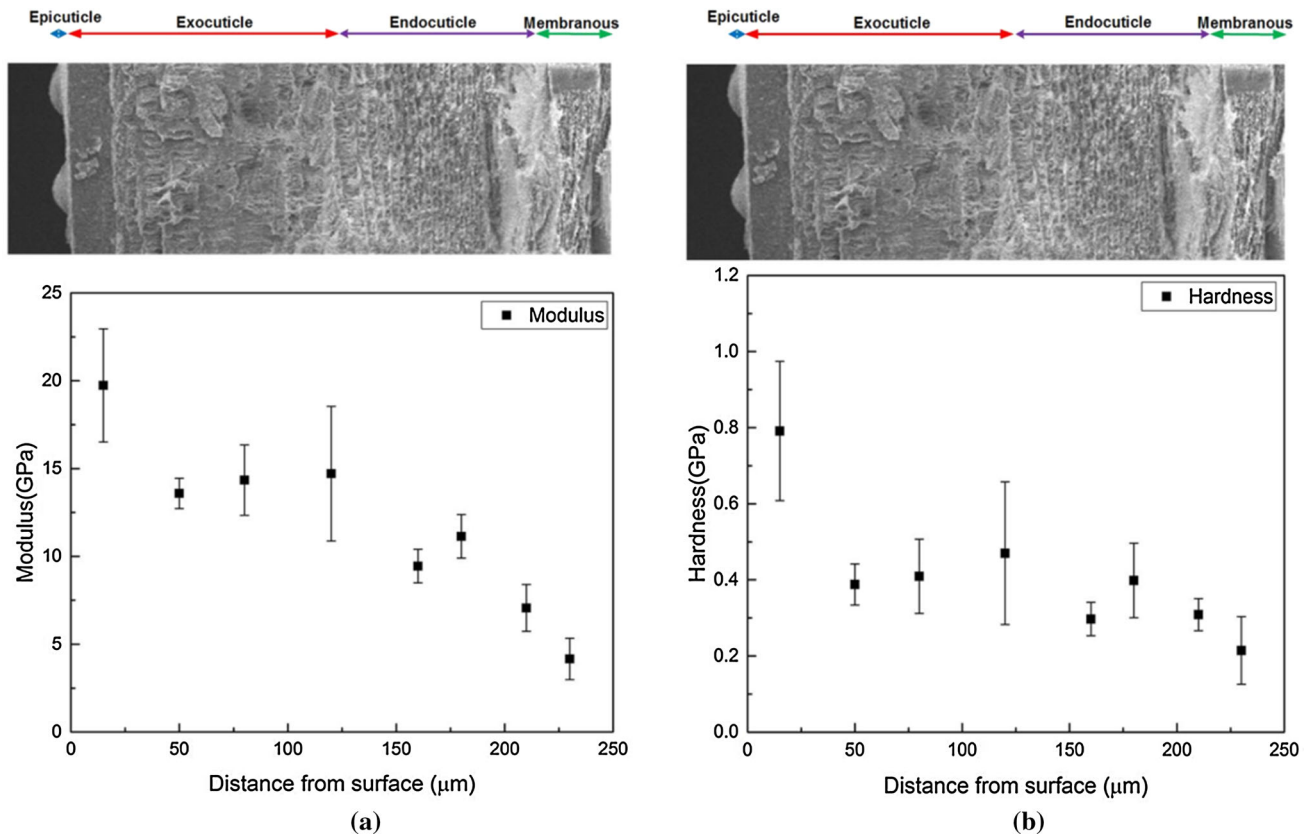


**Figure 9** Averages and standard deviations of the hardness (a) and modulus (b) with respect to the distance from the surface. a Microindentation hardness showing a discontinuity through the thickness of the shrimp claws. The SEM micrograph on the top

respectively. The measurement results showed that both the modulus and hardness along the cross section decrease progressively from the outermost layer to the innermost layer.

### Computational fluid dynamics simulation

The simulation results of the micropapillae model and the smooth model are shown in Fig. 10. The near-wall velocity distribution of water was calculated in the simulation. The near-wall velocity of the turbulent in the micropapillae model was obviously lower than that in the smooth model, as shown in Fig. 10a, b. It was also found that tire-shaped vortices were formed around the surface of the micropapillae model. Compared with the smooth model, the vortices appeared to drastically alter the turbulent near the wall, from sliding friction (seen in the smooth model) to rolling friction, thereby decreasing the wall frictional drag (Fig. 10b). Turbulent kinetic energy, defined as the mean kinetic energy per unit mass

indicates the locations where the indentations were taken; b the changes in the modulus with respect to the distance from the surface.

associated with eddies in a turbulent flow, was also calculated. The turbulent kinetic energy distributions generated by the micropapillae model and the smooth model are shown in Fig. 10c. The turbulent kinetic energy on the top surface was higher for the micropapillae model than that of the smooth model. However, the turbulent kinetic energy in the near-wall region of the micropapillae unit was lower than that of the smooth model, which suggests that the micropapillae units contribute to drag reduction.

### Discussion

Previous investigations have mainly focused on the rapid closure motion pattern, snapping sound and shrimp luminescence of snapping shrimp. The snapping shrimp preys by rapidly closing its snapping claw to generate a fast water jet, creating shockwaves that bombard the nearby prey and other shrimp. Therefore, the snapping shrimp claw

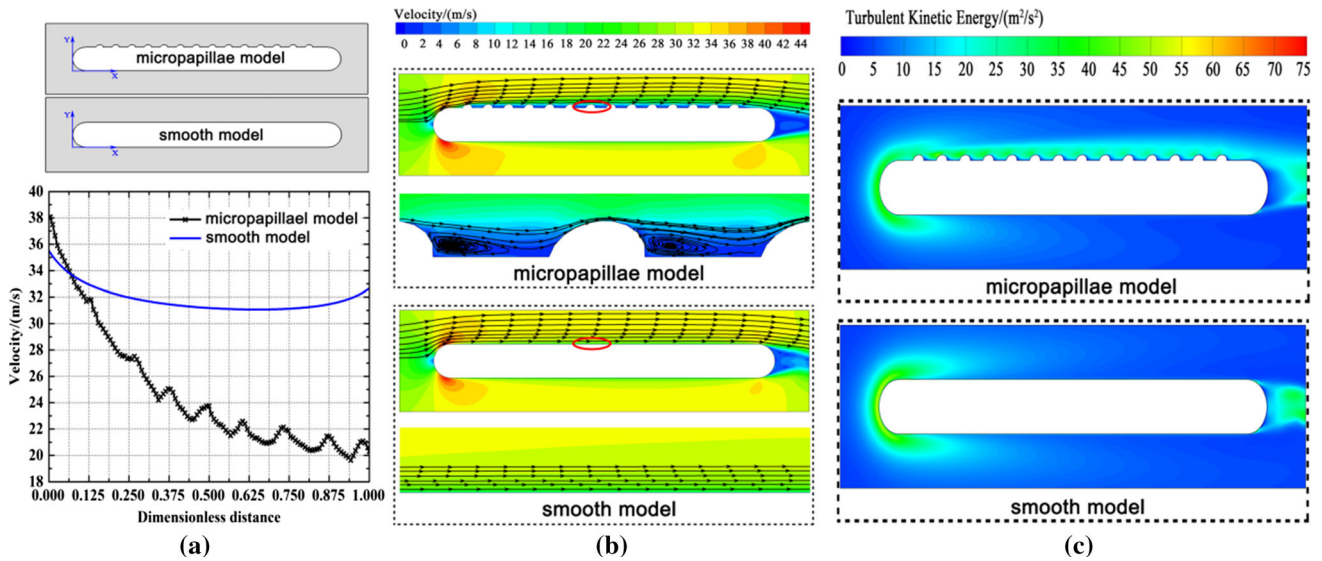


**Figure 10** CFD simulation results generated by the micropapillae model and smooth model. **a** The velocity and dimensionless distance diagram of two different models; **b** simulation results of

the near-wall velocity distribution of water for the micropapillae model and smooth model; **c** turbulent kinetic energy distributions produced by the micropapillae model and smooth model.

requires impact resistance and drag reduction properties.

In this study, experimental measurements of the microstructure, surface morphology, material composition and mechanical properties of the snapping shrimp claw were conducted. The surface of the dactyl and propus was found to consist of cone-shaped micropapillae, rhombic dents and short straight stripes with a hierarchical structure across different scales. This specific morphology has received relatively little attention in previous investigations of crustaceans’ claws, yet it determines the boundaries and interactions between the snapping claw surface and the water. The surface morphology may contribute to the rapid closure of the snapping claw in a manner similar to the skins of sharks and dolphins, which facilitate fast swimming by reducing drag. Previous experimental and modelling investigations have shown that a shark’s high swimming velocity arises not only from its body, which is perfectly streamlined for minimising resistance, but also from the rough microstructure or the interlocked 3D dermal denticles on the surface of its skin [20–22]. It has already been demonstrated that these features of shark skin effectively lift vortices and decrease transverse shear stress and drag [23–27]. In contrast to the shark, the dolphin’s skin surface is very smooth but is embedded with sinusoidal grooves [28]. It has been shown that the compliant dolphin skin can

respond to water flow during swimming, and a non-smooth morphology resulting from the embedded grooves appears on the surface to reduce drag [29–32]. Therefore, to verify the possible drag reduction function of the cone-shaped micropapillae morphology distributed on the surface of the dactyl and propus, CFD simulations of the micropapillae model and the smooth model were conducted in the current study. The CFD results suggested that the cone-shaped micropapillae units play a role in the rapid closure motion of the snapping claw by reducing drag under water. Due to the smaller scales of the rhombic dents and short straight stripes compared with the cone-shaped micropapillae, only the surface model with micropapillae units was analysed. Future work will investigate the effects of the whole hierarchical morphology on claw motion.

The microstructures of the cross section of the snapping claw were obtained in the study. The lamellar fibre-stacked exocuticle and Bouligand-structured endocuticle are the main structural parts of the snapping claw. The exocuticle (except the distal smooth layer) consists of chitin fibres arranged vertically in a lamellar fashion. To the best of our knowledge, this structure has not been reported in the exocuticle layer of other crustacean exoskeletons. The Bouligand-type structure has been found in other biological materials such as the skeletons of crustaceans and beetles, collagen networks of compact

bone and cellulose fibres in plant cell walls [17, 33–35]. Extensive studies have highlighted that this helicoidal structure plays an important role in supporting the animal's body weight, enhancing ductility and toughness and resisting predator attacks and environmental damage [33, 36–38]. Therefore, these lightweight and special structures in the exocuticle and endocuticle could provide the snapping shrimp claw with enhanced mechanical or even heat-impact resistance that protects it during the claw's rapid closure and collapse of the cavitation bubbles.

Nanoindentation measurements of the different layers in the cross section of the snapping claw showed that both the modulus and hardness decrease progressively from the distal smooth layer of the exocuticle to the innermost membranous layer. This pattern is similar to that of the sheep crab claw [39]. However, the calcium content of the exocuticle is lower than that of the endocuticle (Fig. 6). Both layers are composed of stacked chitin–protein fibres. The modulus and hardness gradients of the exocuticle and endocuticle layers may arise from the gradations in different fibre orientations and the stack density [40]. The exocuticle has a lamellar structure and is stacked more densely than the endocuticle layer, as shown in Fig. 4. The discontinuity in the modulus and hardness across different layers has also been found in the crab claw [17] and American lobster [41]. This gradient modulus can effectively suppress microcracks at the interfaces when subjected to external loads [42].

A recent work reported that the ratio between the indentation hardness ( $H_I$ ) and modulus ( $E_I$ ) of biological material is a key parameter that serves as a proxy for the ratio between irreversible and reversible deformation in the contact zone during indentation and the material's yield strength [43] and hence facilitates the quantitative comparison and evaluation of structural biological materials. In this work [43], the elastic index ( $I_E$ ) was determined as

$$I_E = H_I/E_I \quad (1)$$

and the yield strength ( $\sigma_Y$ ) of the material was obtained by the following equations,

$$\sigma_Y = H_I/\gamma \quad (2)$$

$$\gamma = \frac{2A_1}{\tan(\beta)} I_E \frac{1}{a \tanh[2/\tan(\beta)I_E]} \quad (3)$$

where  $A_1$  is a constant depending on the indenter geometry and the yield criterion (for a Berkovich tip and the von Mises yield criterion,  $A_1 \approx 2.75$ ;  $\beta = 19.7^\circ$  [43, 44]). Based on the indentation hardness and modulus data, we calculated the elastic index  $I_E$  and yield strength  $\sigma_Y$  of the surface of the dactyl and propus, and different layers of the cross section of the claw, respectively. From the distal smooth layer of the exocuticle to the innermost membranous layer, the elastic index  $I_E$  was 0.04, 0.03, 0.037 and 0.05, respectively, and for the surface of the dactyl and propus it was 0.08 and 0.07, respectively. All of the obtained  $I_E$  values were within the range of 0.01–0.1, which has previously been determined for biological material [43]. The calculated yield strength of the surface of the dactyl and propus and the four layers from the epicuticle to the membranous was 492, 157 and 292 MPa (epicuticle layer), 151 MPa (exocuticle layer), 129 MPa (endocuticle layer) and 78 MPa (membranous layer), respectively. This implies that the material of the snapping claw becomes much stronger towards the outer surface, thus helping the snapping claw to resist external damage. Therefore, it can be concluded that by combining a few components with differing properties and structuring them in several hierarchical levels, the snapping shrimp has managed to build its snapping claw with materials that are tailored to fulfil specific biological functions. The findings are important for materials scientists and engineers to better understand the material design of the snapping claw and thus develop novel biomimetic materials with enhanced properties, such as drag reduction and impact and crack resistance.

## Conclusions

This study conducted an experimental observation of surface morphology, structure and mechanical properties of the snapping shrimp claw. Cone-shaped micropapillae, rhombic dents and short straight stripes were hierarchically distributed on the surface of the snapping claw. The cone-shaped micropapillae units change the interaction between the turbulent around the wall from sliding friction to rolling friction, resulting in tire-shaped vortices. This reduces the turbulent kinetic energy in the near-wall region, thereby contributing to drag reduction. Four layers,

an epicuticle, exocuticle, endocuticle and membranous layer, were observed in the cross section of the snapping claw. The exocuticle is composed of chitin fibres arranged vertically in a lamellar fashion and the endocuticle has a Bouligand-type structure. This lightweight and unique structure helps the snapping shrimp to mechanically protect the claw during rapid closure. Both the modulus and hardness decrease progressively from the outermost epicuticle to the innermost membranous layer. These modulus and hardness gradients may play key roles in suppressing microcracks at the interfaces between different layers when subjected to external loads.

## Acknowledgements

This work was supported by grants from the National Natural Science Foundation of China (Nos. 51675222 & 51475202), the project on scientific and technological cooperation between China and Italy (No. 2016YFE0103700), the science and technology development planning project of Jilin Province (20180101068JC) and the program for JLU Science and Technology Innovative Research Team. RA is grateful to Jilin University for providing a travel scholarship (111 project) for research collaboration.

## Compliance with ethical standards

**Conflict of interest** The authors declare no conflict of interest.

## References

- [1] Versluis M, Schmitz B, Von der Heydt A, Lohse D (2000) How snapping shrimp snap: through cavitating bubbles. *Science* 289:2114–2117
- [2] Herberholz J, Schmitz B (1999) Flow visualization and high speed video analysis of water jets in the snapping shrimp (*Alpheus heterochaelis*). *J Comp Physiol A* 185:41–49
- [3] Schmitz B, Herberholz J (1998) Snapping movements and laser doppler anemometry analysis of water jets in the snapping shrimp *Alpheus heterochaelis*. In: *Proceedings of the 26th Gottingen Neurobiol. Conf.* 2: 241
- [4] Schmitz B, Herberholz J (1998) Snapping behavior in intraspecific agonistic encounters in the snapping shrimp (*Alpheus heterochaelis*). *J Biosci* 23:623–632
- [5] Lohse D, Schmitz B, Versluis M (2001) Snapping shrimp make flashing bubbles. *Nature* 413:477–478
- [6] Ritzman RE (1974) Mechanisms for the snapping behavior of two Alpheid shrimp, *Alpheus californiensis* and *Alpheus heterochaelis*. *J Comp Physiol* 95(3):217–236
- [7] Brown Kathryn (2000) For certain shrimp, life's a snap. *Science* 289:2020–2021
- [8] Au WWL, Banks K (1998) The acoustics of the snapping shrimp *Synalpheus parneomeris* in Kaneohe Bay. *J Acoust Soc Am* 103:41–47
- [9] Epifanio CL, Potter JR, Deane GB, Readhead ML, Buckingham MJ (1999) Imaging in the ocean with ambient noise: the ORB experiments. *J Acoust Soc Am* 106(6):3211–3225
- [10] McNamara WB, Didenko YT, Suslick KS (1999) Sonoluminescence temperatures during multi-bubble cavitation. *Nature* 401:772–775
- [11] Schultz S, Wuppermann K, Schmitz B (1998) Behavioural interactions of snapping shrimp (*Alpheus heterochaelis*) with conspecifics and sympatric crabs (*Eurypanopeus depressus*). *Zool Anal Complex Syst (Suppl I)* 101:85
- [12] Kaji T, Anker A, Wirkner CS, Palmer AR (2018) Parallel saltational evolution of ultrafast movements in snapping shrimp claws. *Curr Biol* 28:1–8
- [13] Chen PY, Lin AY, McKittrick J, Meyers MA (2008) Structure and mechanical properties of crab exoskeletons. *Acta Biomater* 4:587–596
- [14] Oliver WC, Pharr GM (2004) Measurement of hardness and elastic modulus by instrumented indentation: advances in understanding and refinements to methodology. *J Mater Res* 19(1):3–20
- [15] Shu S, Lu J, Li D (2007) A systematic study of the validation of Oliver and Pharr's method. *J Mater Res* 22(12):3385–3396
- [16] Koutsourakis N, Bartzis JG, Markatos NC (2012) Evaluation of Reynolds stress,  $k-\epsilon$ , and RNG  $k-\epsilon$ , turbulence models in street canyon flows using various experimental datasets. *Environ Fluid Mech* 12:379–403
- [17] Coirier WJ, Fricker DM, Furmanczyk M, Kim S (2005) A computational fluid dynamics approach for urban area transport and dispersion modeling. *Environ Fluid Mech* 5:443–479
- [18] Chan TL, Dong G, Leung CW, Cheung CS, Hung WT (2002) Validation of a two-dimensional pollutant dispersion model in an isolated street canyon. *Atmos Environ* 36:861–872
- [19] Girault V, Raviart PA (1986) Finite element methods for Navier-Stokes equations: theory and algorithms, vol 87. Springer, Berlin, pp 167–204
- [20] Martin S, Bhushan B (2016) Modeling and optimization of shark-inspired riblet geometries for low drag applications. *J Colloid Interface Sci* 474:206–215

- [21] Pu X, Li G, Liu Y (2016) Progress and perspective of studies on biomimetic shark skin drag reduction. *ChemBioEng Rev* 3:26–40
- [22] Chen HW, Zhang X, Ma LX, Che D, Zhang DY, Sudarshan TS (2014) Investigation on large-area fabrication of vivid shark skin with superior surface functions. *Appl Surf Sci* 316:124–131
- [23] Bixler GD, Bhushan B (2013) Fluid drag reduction with shark-skin riblet inspired microstructured surfaces. *Adv Funct Mater* 23:4507–4528
- [24] Dean B, Bhushan B (2010) Shark-skin surfaces for fluid-drag reduction in turbulent flow: a review. *Philos Trans R Soc Lond A* 368:4775–4806
- [25] Bixler GD, Bhushan B (2013) Shark skin inspired low-drag microstructured surfaces in closed channel flow. *J Colloid Interface Sci* 393:384–396
- [26] Afroz F, Lang A, Habegger ML, Motta P, Hueter R (2016) Experimental study of laminar and turbulent boundary layer separation control of shark skin. *Bioinspir Biomim* 12(1):016009
- [27] Afroz F, Sharif MA, Lang A (2016) Numerical study of adverse pressure gradient generation over a flat plate using a rotating cylinder. *J Fluids Struct* 62:187–208
- [28] Lang AW, Jones EM, Afroz F (2017) Separation control over a grooved surface inspired by dolphin skin. *Bioinspir Biomim* 12:026005
- [29] Liu E, Li L, Wang G, Zeng Z, Zhao W, Xue Q (2017) Drag reduction through self-texturing compliant bionic materials. *Sci Rep* 7:40038
- [30] Fish FE (2006) The myth and reality of Gray's paradox: implication of dolphin drag reduction for technology. *Bioinspir Biomim* 1:R17–R25
- [31] Gad-el-Hak M (2002) Compliant coatings for drag reduction. *Prog Aerosp Sci* 38:77–99
- [32] Bandyopadhyay PR, Hellum AM (2014) Modeling how shark and dolphin skin patterns control transitional wall-turbulence vorticity patterns using spatiotemporal phase reset mechanisms. *Sci Rep* 4:6650
- [33] Weaver JC, Milliron GW, Miserez A, Evans-Lutterodt K, Herrera S, Gallana I, Mershon WJ, Swanson B, Zavattieri P, DiMasi E, Kisailus D (2012) The stomatopod dactyl club: a formidable damage-tolerant biological hammer. *Science* 336:1275–1280
- [34] Bouligand Y (1972) Twisted fibrous arrangements in biological materials and cholesteric mesophases. *Tissue Cell* 4:189–217
- [35] Weiner S, Addadi L (1997) Design strategies in mineralized biological materials. *J Mater Chem* 7:689–702
- [36] Yang RG, Zaheri A, Gao W, Hayashi C, Espinosa HD (2017) AFM identification of beetle exocuticle: bouligand structure and nanofiber anisotropic elastic properties. *Adv Funct Mater* 27:1603993
- [37] Yaraghi NA, Guarín-Zapata N, Grunenfelder LK, Hintsala E, Bhowmick S, Hiller JM, Betts M, Principe EL, Jung JY, Sheppard L, Wuhner R, McKittrick J, Zavattieri PD, Kisailus D (2016) A sinusoidally architected helicoidal biocomposite. *Adv Mater* 28:6835–6844
- [38] Zimmermann EA, Gludovatz B, Schaible E, Dave NK, Yang W, Meyers MA, Ritchie RO (2013) Mechanical adaptability of the Bouligand-type structure in natural dermal armour. *Nat Commun* 4:2634
- [39] Chen PY, Lin AY, Lin YS, Seki Y, Stokes AG, Peyras J, Olefsky EA, Meyers MA, McKittrick J (2008) Structure and mechanical properties of selected biological materials. *J Mech Behav Biomed Mater* 1:208–226
- [40] Lian J, Wang J (2014) Microstructure and mechanical anisotropy of crab cancer magister exoskeletons. *Exp Mech* 54:229–239
- [41] Raabe D, Sachs C, Romano P (2005) The crustacean exoskeleton as an example of a structurally and mechanically graded biological nanocomposite material. *Acta Mater* 53:4281–4292
- [42] Suresh S (2001) Graded materials for resistance to contact deformation and damage. *Science* 292(5526):2447–2451
- [43] Labonte D, Lenz AK, Oyen ML (2017) On the relationship between indentation hardness and modulus, and the damage resistance of biological materials. *Acta Biomater* 57(15):373–383
- [44] Yu W, Blanchard JP (1996) An elastic-plastic indentation model and its solutions. *J Mater Res* 11(09):2358–2367